High-Velocity Air–Water Flow Measurements in a Prototype Tunnel Chute: Scaling of Void Fraction and Interfacial Velocity

Journal Article

Author(s):
Hohermuth, Benjamin (iD); Boes, Robert (iD); Felder, Stefan

High-Velocity Air-Water Flow Measurements in a Prototype Tunnel Chute: Scaling of Void Fraction and Interfacial Velocity

B. Hohermuth[a,*], R.M. Boes[b], S. Felder[c]

[a] *Postdoctoral Researcher, Laboratory of Hydraulics, Hydrology and Glaciology (VAW), ETH Zurich, Switzerland, ORCID 0000-0001-8218-0444. Email: hohermuth@vaw.baug.ethz.ch*
[b] *Professor, Director, Laboratory of Hydraulics, Hydrology and Glaciology (VAW), ETH Zurich, Switzerland, ORCID 0000-0002-0319-976X*
[c] *Senior Lecturer, Water Research Laboratory, School of Civil and Environmental Engineering, UNSW Sydney, Australia, ORCID 0000-0003-1079-6658*

Abstract

Aeration occurs in many natural and human-made flows and must be considered in engineering design. In water infrastructure, air-water flows can be violent and of very high velocity. To date, most fundamental research and engineering design guidelines involving air-water flows have been based upon laboratory scale measurements with limited validation at prototype scale with larger Reynolds numbers. Herein, unique measurements were conducted in high-velocity air-water flows in the tunnel chute of the 225 m high Luzzone arch dam in Switzerland. For each of the two test series an array of 16 double-tip conductivity probes was installed in the circular tunnel chute of 3 m diameter and slope of $\approx 37°$ measuring void fraction, bubble count rate, interfacial velocity and droplet sizes for four different discharges of up to 15.9 m^3/s corresponding to Reynolds numbers of up to $2.4 \cdot 10^7$ and mean flow velocities of up to 38 m/s. Void fraction and interfacial velocity distributions, as well as design parameters such as depth-averaged void fractions and flow resistance compared well with previous laboratory studies and empirical equations. The droplet chord sizes exhibited scale effects and care must be taken if air-water mass transfer and droplet momentum exchange processes are assessed at laboratory scale.

Keywords: Air-water flow, Droplet size, Prototype measurements, Phase-detection probes, Scale effects

1. Introduction

Air-water flows occur in natural waterways such as river rapids and in human-made water infrastructure including flow conveyance and energy dissipation structures. While air-water flows in wastewater treatment and process engineering typically involve relatively low flow velocities, high-velocity air-water flows are commonly found in spillways with different invert-roughness (e.g. smooth or stepped), various cross-sections (mostly of rectangular shape, but sometimes trapezoidal or circular and even non-prismatic), different slopes and length, as well as with or without spillway aerator. In high-velocity flows, flow aeration is a dominant feature and must be considered in design guidelines of water infrastructure.

Fundamental research of high-velocity air-water flows has provided insights into the entrainment process (Wood, 1991; Chanson, 1997; Brocchini and Peregrine, 2001; Toro et al., 2017; Valero and Bung, 2018), the intense interactions between air and water entities (Felder and Chanson, 2016a), the air-water flow properties at macro- and microscopic scale (Chanson and Toombes, 2002; Felder and Chanson, 2015b) as well as the flow's turbulence (Kramer et al., 2020). Numerous studies focused upon design parameters including smooth-invert spillways (Straub and Anderson, 1958; Cain and Wood, 1981; Kramer et al., 2006), stepped spillways (Matos, 2000; Boes and Hager,

2003a; Hunt et al., 2014; Felder and Chanson, 2016b), block ramps (Hartung and Scheuerlein, 1970; Pagliara et al., 2010) and tunnel chutes (Speerli and Hager, 2000; Hohermuth, 2019). Most air-water flow studies were conducted at laboratory scale with Reynolds numbers $10^5 \lesssim \mathsf{R} \lesssim 3 \cdot 10^6$, where $\mathsf{R} = 4R_h U_{m,w}/\nu$, with R_h the hydraulic radius based on the equivalent clear-water flow depth Y_w, $U_{m,w}$ the cross-sectional average water velocity and ν the kinematic water viscosity. Table 1 summarizes studies of high-velocity air-water flows comprising laboratory studies with the largest Reynolds numbers and flow velocities as well as the few available prototype studies. At prototype scale, air-water flows may occur at Reynolds numbers exceeding 10^7 to 10^8 (Chanson, 2015), while most laboratory-scale studies have been conducted at Reynolds numbers of 1 to 3 magnitudes lower (Table 1). Small scale models may also hide important air-water flow features that can only be observed at full scale as shown in a laboratory study of the nappe flow regime on a stepped spillway with prototype-scale steps height (Felder et al., 2019a).

Scale effects are a common issue in air-water flows (Kobus, 1984; Wood, 1991; Heller, 2011) which may affects the extrapolation of laboratory scale design guidelines and air-water mass, momentum and heat transfer processes to the prototype scale. Experimental evidence of high-velocity flows on stepped spillway suggests $\mathsf{R} \gtrsim 4 \cdot 10^5$ (assuming $Y_w \approx R_h$) to prevent scale effects in terms of void fraction and interfacial velocity for Froude models (Boes and Hager, 2003b). In Froude mod-

---

*Corresponding author

Table 1: Prototype studies and selected laboratory studies of high-velocity air-water flows with largest measured flow velocities and Reynolds numbers to date. [1]R estimated with $R_{h,w} \approx Y_w$, with Y_w the equivalent clear-water depth. [2]R calculated with $\nu = 1.2 \cdot 10^{-6}$ m²/s (corresponding to $\approx 12°$C), $\nu = 1 \cdot 10^{-6}$ m²/s was used for all other studies.

Reference	Type of air-water flow	Instrumentation	R = $4R_h U_m / \nu$ (-)	U (m/s)
Straub and Anderson (1958)	Smooth spillway laboratory model	Conductivity probe for C	$4.7 \cdot 10^5$ to $2 \cdot 10^6$	3.7 to 16.4
Keller (1972); Keller et al. (1974)	Smooth spillway (Aviemore Dam, NZ)	Conductivity probe for C	$9.0 \cdot 10^6$ to $2.7 \cdot 10^7$	N/A
Cain (1978); Cain and Wood (1981)	Smooth spillway (Aviemore Dam, NZ)	Conductivity probe for C ($\varnothing_o = 6$ mm), double-tip conductivity probe for U ($\varnothing_o = 1$ mm)	$8.9 \cdot 10^6$ to $1.3 \cdot 10^7$	12 to 22
Volkart and Rutschmann (1984)	Smooth tunnel spillway (Grande Dixence, CH)	Conductivity probe for C ($\varnothing_o = 0.5$ mm), pitot tube for U	$7.1 \cdot 10^6$ to $1.1 \cdot 10^7$	10 to 22
Pujol et al. (1985); Vernet et al. (1988)	Smooth spillway with aerators (Alicura Dam, AR)	Flat plate capacitor for C_b	$2.3 \cdot 10^7$ to $9.4 \cdot 10^7$ [1]	N/A
Aivazyan (1986)	Concrete spillway (Ak-Tepe, USSR)	Measurement of water saturation coefficients and velocities	$8.8 \cdot 10^6$ to $2.8 \cdot 10^7$	13 to 20
Speerli (1999); Speerli and Hager (2000)	Open channel downstream of sluice gate laboratory model	Serial conductivity probe for U ($\varnothing_o = 6$ mm), single-tip conductivity probe for C ($\varnothing_o = 1.5$ mm)	$5.3 \cdot 10^5$ to $3.7 \cdot 10^6$	4 to 20
Boes and Hager (2003a,b)	Stepped spillway laboratory model	Double-tip fibre-optical probe ($\varnothing_o = 0.1$ mm)	$2.2 \cdot 10^5$ to $1.1 \cdot 10^6$	up to ≈ 7
Felder et al. (2019b); Hohermuth (2019)	Low-level outlet laboratory model	Double-tip conductivity probe ($\varnothing_o = 0.6$ mm; $\varnothing_i = 0.125$ mm)	$6.6 \cdot 10^5$ to $3.2 \cdot 10^6$	4 to 22
Present study	Smooth tunnel spillway (Luzzone Dam, CH)	Double-tip conductivity probe ($\varnothing_o = 0.6$ mm; $\varnothing_i = 0.125$ mm)	$7.8 \cdot 10^6$ to $2.4 \cdot 10^7$ [2]	23 to 38

els, criteria to limit scale effects for air demand in aerators and void fraction and velocity distributions in hydraulic jumps have also been published (Pfister and Chanson, 2012, 2014; Chanson and Gualtieri, 2008). In terms of particle count rates and particle sizes, significant scale effects were identified for stepped spillway flows with $8.1 \cdot 10^4 \leq R \leq 9 \cdot 10^5$ (Felder and Chanson, 2009, 2017), tunnel chutes with $2.7 \cdot 10^5 \leq R \leq 2.2 \cdot 10^6$ (Hohermuth, 2019), and hydraulic jumps with $2.7 \cdot 10^5 \leq R \leq 2.2 \cdot 10^6$ (Chanson and Chachereau, 2013; Wang and Chanson, 2016). Particle sizes and quantities do not scale within the range of typical laboratory experiments and are unlikely to scale to even larger Reynolds numbers at prototype scale. While laboratory based studies of scale effects have provided some important guidance, there is currently no confirmation on the possibility to scale air-water flow properties of any laboratory study to the prototype scale (Chanson, 2015).

Prototype scale experiments of high-velocity flows have been limited (Table 1). Several studies have observed the inception point of free-surface aeration remotely (e.g. Keller et al. (1974); Cain (1978)), or estimated local flow properties comprising the average flow velocity and the flow depth visually, (e.g. Hall (1943); Aivazyan (1986)). Direct measurements of air-water flows on a prototype spillway are currently limited to research by Keller (1972); Keller et al. (1974) and Cain (1978); Cain and Wood (1981) on the Aviemore Dam spillway measuring the local void fraction and velocity. However, the Aviemore data are limited to void fraction and velocities of up to 22 m/s and within the developing flow region. Herein, we measured air-water flow properties including void fraction, particle count rate, chord sizes and interfacial velocities intrusively in a prototype tunnel chute with uniform flow conditions for $R = 2.4 \cdot 10^7$. The prototype results were compared with laboratory observations including the tunnel chute data of Felder et al. (2019b); Hohermuth (2019) providing a validation of previous laboratory scale research.

2. Prototype tests

Luzzone is an arch dam in Switzerland initially constructed in 1963 and raised in 1997/98 to its final height of 225 m. It features three outlets, a tunnel spillway, a middle (MO) and a bottom outlet (BO) (Fig. 1a). The chute of the MO starts with a chute angle of $\theta \approx 20°$ and takes a parabolic shape in longitudinal profile for roughly 50 m before it merges with the tunnel spillway with $\theta \approx 37°$. Further downstream, the tunnel spillway is joined by the BO. The measurements were conducted towards the downstream end of the inclined part of the tunnel spillway (cross-section B in Fig. 1a).

Two measurement campaigns were conducted in 2019 and 2020, referred to as "T1" and "T2", respectively. After successful measurements in 2019, the instrumentation of the second test series was further optimised.

2.1. Test series T1 in 2019

An array of 16 double-tip phase-detection conductivity probes (CP) was attached to a 1.5 m high vertically installed stainless steel beam (Fig. 1b, c). The probes were placed in the tunnel centerline and equally spaced 0.09 m apart in the vertical direction starting at 0.11 m away from the invert. The CP were manufactured at the Water Research Laboratory (WRL) at UNSW Sydney, Australia. The design was similar to probes used in high-velocity model studies (Felder et al., 2019b; Hohermuth, 2019) with two needle tips with outer and inner electrodes with diameters of $\varnothing_o = 0.6$ mm and $\varnothing_i = 0.125$ mm, respectively. The streamwise separation distance of the probe tips (Δx) varied between 4 and 5 mm and was measured with a microscope with ± 0.02 mm accuracy for each probe. A National Instruments USB-6349 Multifunction I/O device was used to sample the raw voltage signal with 100 kHz for each of the 32 probe tips. The data were stored locally on a fanless computer placed inside a waterproof data acquisition (DAQ) box (Fig. 1f). The

DAQ was accessed remotely during the measurement and controlled using a LabVIEW environment.

Measurement campaign T1 was conducted during an annual sediment flushing operation on October 21, 2019. During the flushing operation the BO was operated at different gate openings for a few minutes up to several hours to release water and sediment. Additional, supposedly sediment-free water was released from the MO to dilute the downstream suspended sediment concentrations and minimise adverse ecological effects. The BO and MO gate openings were controlled by the dam operator based on sediment mobilization and downstream suspended sediment concentrations. During this operation, the array of CP was exposed to the clear-water flows in the tunnel chute downstream of the MO. Most of the CP failed at some point during the test campaign. Two main types of probe failure were observed: (i) near-instant change from good signal quality to unusable readings, and (ii) gradual deterioration of the signal through increasing noise. The former was likely due to debris impact; this was most prevalent during the first few minutes of the release when debris particles deposited in the MO tunnel as well as furnace slag used to seal the service gate were mobilized. Some probes showed significant damage with both needles completely teared off, while others only showed damage to the inner electrodes. Mechanism (ii) was likely attributed to flow-induced vibrations of the needles creating cracks in the insulating epoxy layer between inner and outer electrode. The affected probes showed increasing noise and sometimes even negative voltage spikes which may have been caused by water intrusion into the epoxy insulation turning the needle into a capacitor and eventually short-circuiting the probe. For some probes this deterioration occurred in spurts, i.e., rapid signal degradation within less than a minute followed by a stabilization at a lower level (e.g. the voltage span between water and air was reduced compared to the original signal) for several minutes. The prototype measurements provided usable data series for three discharges $Q_w = 3.2$ m^3/s (duration $\approx$ 10 min), $Q_w = 9.7$ m^3/s (duration $\approx$ 6 min) and $Q_w = 13.0$ m^3/s (duration $\approx$ 25 min) (Fig. 2a-d). The duration refers only to steady state conditions (i.e. transitions between flow stages were excluded). The discharge was estimated as $Q_w = C_c\, a\, w\, \sqrt{2g(H - C_c\, a)}$, with a = gate opening, w = gate width, C_c = contraction coefficient and H = hydraulic head. The hydraulic head was provided by the dam operator as the difference between water level and gate invert and C_c was based on model tests for the Luzzone BO gate with a geometry similar to the MO gate. As a significant change in signal quality (e.g. the voltage span between water/air) can negatively affect the signal analysis (e.g. threshold selection), a 2 min segment of high data quality was selected by visual inspection of the raw Voltage signals and Voltage histograms. The selected 2 min were long enough to achieve converged results regarding time-averaged void fraction and velocity but short enough to limit effects of probe deterioration. The procedure was validated by comparing two further 2-minute segments for $Q_w = 9.7$ m^3/s, revealing consistent results in terms of raw data histograms and air-water flow properties.

2.2. Test series T2 in 2020

Data close to the invert was lacking from the T1 test series due to the destruction of most CP with $y < 0.3$ m by debris impact during the first surge. Therefore, the campaign T2 aimed to collect more data in this region. To achieve this, the length of the stainless steel beam was reduced to 1 m and the CP were spaced more closely near the invert (Fig. 1a, d); starting at $y = 0.04$ m with a spacing of 0.03 m increasing to 0.09 m towards the top. Additionally, the probe sturdiness was increased by (i) increasing the outer electrode diameter to $\varnothing_o = 0.8$ mm, (ii) soldering leading and trailing needles together into a support sleeve, and (iii) reducing the streamwise separation to $\Delta x \approx 2$ mm (Fig. 1e). An upgrade of the DAQ allowed to increase the sampling rate of the raw voltage signal to 500 kHz for each of the 32 probe tips.

The campaign T2 was conducted on August 29, 2020 again during a sediment flushing operation. The tests were initiated with a small flow (≤ 1 m^3/s) held for ≈ 10 min to flush out small debris at a reduced risk of probe damage. Afterwards, favourable hydrological conditions allowed a maximum discharge of $Q_w = 15.9$ m^3/s at the start of the campaign for ≈ 75 min, which was then lowered to $Q_w = 12.7$ m^3/s for ≈ 60 min (Fig. 2e, f). Despite the effort to flush debris at the start of the test, most CP failed during the first few minutes, probably due to the mobilisation of additional debris with increasing discharge. Nevertheless, two CP located at $y < 0.3$ m remained operational. Probes spared by debris impact showed slower signal degradation, likely due to less flow-induced probe vibration owing to the sturdier design. This allowed to select 5 min data segments of constant data quality for $Q_w = 15.9$ m^3/s and $Q_w = 12.7$ m^3/s. The flushing operation was concluded by increasing the discharge to $Q_w = 19.3$ m^3/s to rinse sediments out of the river bed. Unfortunately, the increased discharge led to water intrusion rendering the DAQ unusable and no data could be recorded at this discharge.

2.3. Data processing

The selected raw Voltage signals of all CP were post-processed using the adaptive window cross-correlation (AWCC) technique with 15 particles per window (Kramer et al., 2019, 2020), providing the local time-averaged void fraction C, the particle count rate F, the chord times of the air and water entities $t_{ch,a}$, $t_{ch,w}$, respectively, and a velocity time series allowing an unbiased estimate of the time-averaged interfacial velocity U (Kramer et al., 2021). The AWCC technique typically applies a single threshold of 50% of the bimodal Voltage distribution peaks to obtain a binarized air-water signal. For the lowermost CP ($y = 0.06$ m) of the T2 tests, strong noise resulted in an indistinct lower Voltage peak for the leading tip and the Voltage threshold was set manually to 3.5 V. This led to consistent results between leading and trailing tip signals.

A review of available accuracy information of CP, indicated accuracy in terms of void fraction of +2% to −6% for the most comparable flow conditions (Kramer et al., 2020). The accuracy of the particle frequency depends on the measurement frequency and the probe diameter, and some implications of the
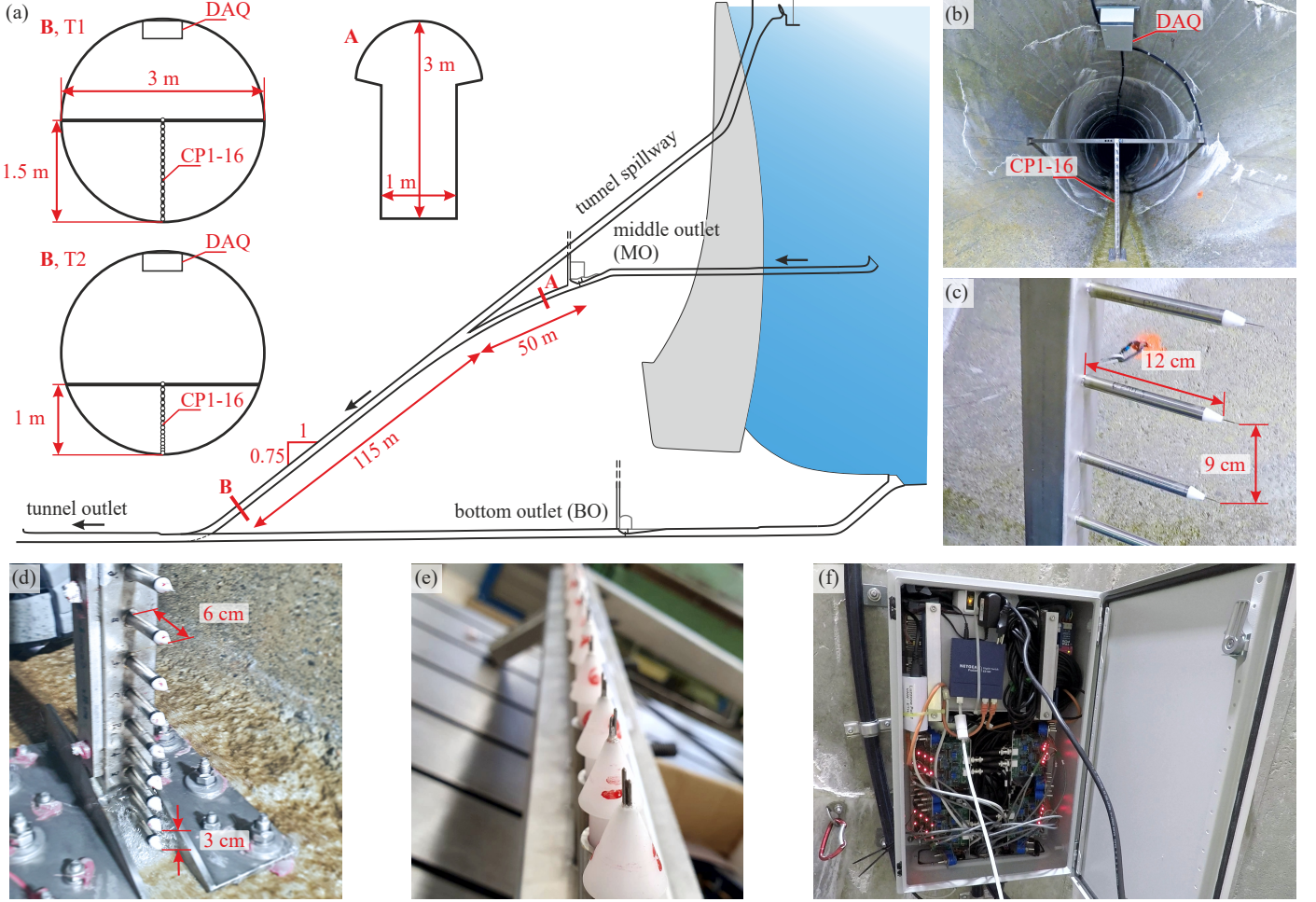
Figure 1: Prototype test setup, (a) longitudinal section of the Luzzone prototype site with cross-sections at different locations, B = measurement location. (b) Overview of installed conductivity probes (CP), support beam and data acquisition box (DAQ) for T1; (c, d) detail of CP array for T1, T2; (e) probe details for T2; (f) closeup of DAQ during installation.

measurement frequency are discussed in the section on particle size distribution. Under laboratory conditions, the uncertainty regarding U is roughly ±5% (Kramer et al., 2020), while for prototype conditions the uncertainty may be slightly larger. The discharge is estimated to be accurate within ±5%.

3. Results

3.1. Basic air-water flow properties

All measured air-water flow properties are shown in Figure 3 comprising dimensional and dimensionless summary plots of void fraction (Fig. 3a and d), particle count rate (Fig. 3b and e) and interfacial velocity (Fig. 3c and f). In the non-dimensional plots, the elevation y was normalised using the characteristic flow depth Y_{90}, i.e. the depth where $C = 0.9$. The particle count rate was normalised using F_{max}, i.e. the maximum particle count rate in a cross-section, and U_{90}, i.e. the characteristic velocity corresponding to $C = 0.9$, is used for the normalisation of the velocity. All void fraction distributions showed S-shapes albeit with limited data points close to the tunnel chute

invert due to missing functional instrumentation after debris impact on the lowest CP. The measured void fraction highlighted significant aeration throughout the water column with a slight trend towards lower aeration for higher discharges. Overall, the void fraction distribution resembled data from laboratory scale experiments with high flow velocities, (e.g. Straub and Anderson (1958); Felder et al. (2019b)). Despite limited data close to the chute invert, the distributions of C were well correlated with the advection-diffusion equation (Eq. 1) for air bubbles (Fig. 3a and d) assuming a constant diffusivity D' across the flow depth (Chanson, 1997):

$$C = 1 - \tanh^2\left(K' - \frac{y/Y_{90}}{2D'}\right) \qquad (1)$$

where D' is the dimensionless diffusivity and K' an integration constant $K' = \tanh^{-1}(0.1^{0.5}) + 1/(2D')$ (for values of D', see Table 2). The mean air concentration C_m was calculated by integrating Eq. 1 leading to:

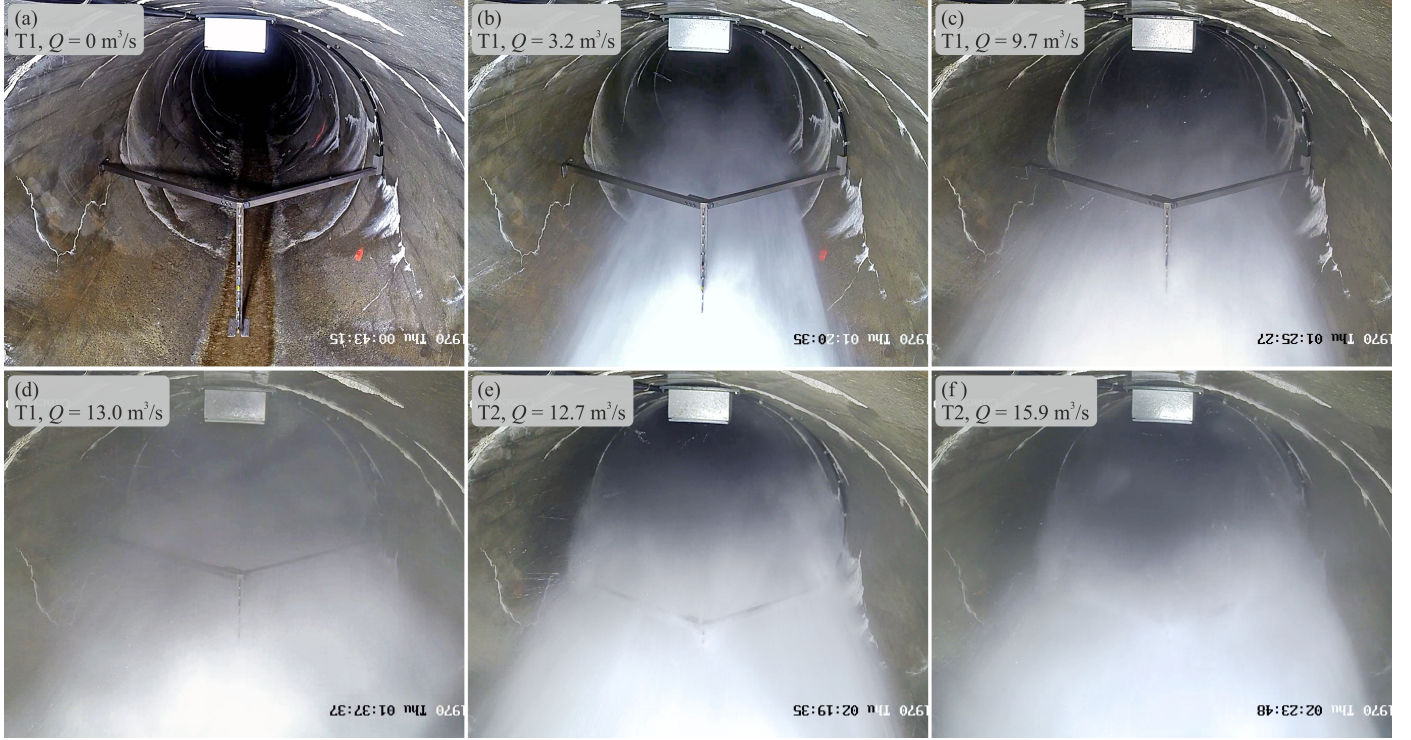$$C_m = 2D'\left(\tanh\left(\sqrt{0.1} + \frac{1}{2D'}\right) - \sqrt{0.1}\right) \qquad (2)$$

4

Figure 2: Photos of array of CP positioned in high-velocity air-water flows for different discharges during (a)-(d) test series T1 and (e),(f) test series T2; view in flow direction.

The close fit of measured void fractions with Eq. 1 suggests that the void fraction distributions and the cross-sectional average air concentration can be accurately scaled between laboratory and prototype up to $Re = 2.4 \cdot 10^7$. Note that the mean air concentration slightly decreased with increasing discharge; this is discussed in detail in the section on air-water bulk properties.

The particle count rate distributions (Fig. 3b and e) showed intense interactions of air and water entities with particle count rates of up to $F \approx 3500$ Hz for T1 and $F \approx 6000$ for T2. The shapes of the F distributions were typical for high-velocity flows with maximum values within the intermediate flow region ($0.3 < C < 0.7$) as commonly observed in laboratory scale high-velocity air-water flows. Note, however, that the maximum particle count rates in T1 were slightly smaller compared to the laboratory experiments of Felder et al. (2019b). While the prototype measurements had higher flow velocity, the sampling rate of 100 kHz per channel for T1 did not allow to measure the actual particle count rate, because particle chords below $L_{ch} \approx 0.4$ mm were not registered by the DAQ. In contrast, during series T2 each probe tip was sampled at 500 kHz per probe tip (similar to the laboratory study of Felder et al. (2019b)) allowing a more complete measurement of the particle count rate (sampling limit at $l_{ch} \approx 0.1$ mm). For example, the measurements for $Q_w = 12.7$ m^3/s (sampled at 500 kHz during T2) showed larger F values compared to $Q_w = 13.0$ m^3/s (sampled at 100 kHz during T1). Comparing F values for the same C between T2 and comparable laboratory scale flows (Hohermuth, 2019), indicated $\approx 50\%$ larger bubble count rates (for $C > 0.6$) corresponding to smaller particle sizes at pro-

totype scale. A more detailed comparison of particle sizes at laboratory and prototype scale is presented in the next section.

Assuming constant and equal bubble and droplet sizes within a cross-section, the relation between particle count rate F and void fraction C can be expressed as (Chanson and Toombes, 2002):

$$\frac{F}{F_{max}} = 4C(1 - C) \tag{3}$$

where F_{max} is the maximum particle frequency within a cross-section, usually occurring for $C \approx 0.5$. Despite the limitation due to the sampling frequency for series T1, all relative particle count rate distributions were well correlated by Eq. 3 (Fig. 3b and e).

The dimensional interfacial velocity distributions (Fig. 3c) highlighted the nature of the high-velocity flows in the prototype tunnel chute with velocities almost twice as large compared to the previously largest measured air-water flow velocities (Table 1). Herein, the data provided unique insights into air-water flows at such velocities. Irrespective of the velocity magnitude, the interfacial velocity distributions followed a power law:

$$\frac{U}{U_{90}} = \left(\frac{y}{Y_{90}}\right)^{1/n} \tag{4}$$

where n is typically $n \approx 6$ for smooth spillways (Chanson, 1997; Cain, 1978), $n \approx 6.3 - 10$ for stepped spillways depending on θ (Boes, 2000; Felder and Chanson, 2016b) and up to $n \approx 12$ for wall jets (Chanson and Brattberg, 2000). The present data were closely reproduced with $n = 6$ (Fig. 3c, f) except for

5

the data point closest to the invert for $Q_w = 15.9$ m³/s. Reduced accuracy in near-invert measurements were also reported in model studies due to increased transverse and vertical velocity fluctuations (Kramer et al., 2020). The probe geometry used in series T2 may have also contributed to inaccuracy in velocity measurements for $C \lesssim 0.7$, as shown in Felder et al. (2019b).

For $y/Y_{90} > 1$, the interfacial velocities were close to unity (i.e. $U/U_{90} \approx 1$) as previously reported in laboratory experiments on stepped chutes (Boes and Hager, 2003b; Felder and Chanson, 2016b). The close agreement between laboratory and prototype observations is decisive since it indicates that important design parameters may be scalable for $R < 2.4 \cdot 10^7$. The large velocities of the ejected droplets for $y \gtrsim Y_{90}$ could have implications for air demand in tunnel chutes since a significant transfer of momentum from droplets to the air superlayer occurs in the upper part of the flow.

3.2. Bulk air-water flow parameters of engineering interest

The void fraction data were used to calculate several characteristic flow parameters including the dimensionless diffusivity D' (Eq. 1), the depth-averaged void fraction C_m (Eq. 2), the equivalent clear water flow depth Y_w, the cross-sectional average flow velocity $U_{m,w}$ and the hydraulic radius R_h (Table 2). To account for the circular cross-section, R_h was calculated based upon the equivalent clear-water cross-section defined as $A_w = A_{90}(1 - C_m)$, with A_{90} the cross-sectional area of the mixture flow up to the elevation Y_{90}. Table 2 shows close agreement between the cross-sectional average velocity $U_{m,w}$ calculated based upon the void fraction data and the mean velocity $\overline{U}$ obtained from Eq. 4 fitted to the measured flow velocities (Fig. 3c), except for the smallest and largest discharge. For $Q_w = 3.2$ m³/s, only one data point was used to obtain U_{90} (and only two for C_m) thus a larger uncertainty is expected. For $Q_w = 15.9$ m³/s, the comparably small $U_{m,w}$ is due to the lower C_m as discussed below.

The bulk air-water flow parameters were compared with previous laboratory scale data and empirical formula. Figure 4a, shows the present results of C_m together with the present bottom air concentrations C_b which were extrapolated from the fit with the advective diffusion equation (Fig. 3a) to the same y as in the data of Straub and Anderson (1958). C_m and C_b are compared with data of Straub and Anderson (1958) for a range of chute angles θ and the empirical approach of Hager (1991):

$$C_m = C_b + 1.05(0.9 - C_b)\left(0.45\sin(\theta)^{0.5}\right) \quad (5)$$

where the bottom air concentration is

$$C_b = 1.25(\theta\pi/180°)^3 \text{ for } 0° \le \theta \le 40° \quad (6a)$$
$$C_b = 0.65\sin(\theta) \text{ for } 40° < \theta < 80° \quad (6b)$$

Overall, the present prototype data compared well with the data of Straub and Anderson (1958) as well as the approach of Hager (1991) providing confidence in the scalability of bulk aeration parameters to prototype chutes with up to $R = 2.4 \cdot 10^7$. However, a trend of decreasing C_m, C_b with increasing discharge was observed - especially for the largest discharge (Fig. 4a). Similar trends were reported for scale model studies of smooth (Straub and Anderson, 1958) and stepped spillways (Felder and Chanson, 2015a). Wood (1991) labelled lower C_m, C_b data from Straub and Anderson (1958) as non-uniform flow, while Straub and Anderson (1958) ensured uniform conditions for all reported C_m, C_b data by checking C profiles at different streamwise locations. The present data were observed in uniform flows for all flow conditions, while non-uniform flow conditions with larger C_m, C_b would be expected in the decelerating flows downstream of the gate. A possible explanation for the decrease in C_m, C_b with increasing discharges in uniform flows are 3D flow effects (Zünd, 2008). Indeed, data from Straub and Anderson (1958) with lower void fractions tend to have aspect ratios $W/Y_{90} \lesssim 5$ (with W = chute width) which are typically associated with the onset of the velocity dip phenomenon (Auel et al., 2014). The resulting secondary currents may redistribute entrained air within the cross-section or affect the overall amount of entrained air. The effect of flow depth (i.e. aspect ratio) on air-water flow properties in high-velocity flows requires further research. In addition, the present data are only available for a single slope ($\theta \approx 37°$) and conventional spillway roughness ($k_s \approx 3$ mm, estimated based upon visual inspection of the concrete chute), and consequently further full-scale data must be collected to confirm the present findings for a range of slopes, roughness heights and even larger Reynolds numbers.

The flow resistance is another important design parameter which is typically expressed by the Darcy-Weisbach friction factor (Chanson, 1994). In air-water flows, the equivalent Darcy-Weisbach friction factor f_a must be used which is calculated with the hydraulic radius $R_{h,w}$ based upon equivalent clear water flow data:

$$f_a = \frac{8gR_{h,w}\sin\theta}{U_{m,w}^2} \quad (7)$$

The flow resistance f_a was calculated using the measured values of $R_{h,w}$ and $U_{m,w}$ (Table 2), while f was calculated assuming non-aerated uniform flow conditions at the measurement location. The ratio f_a/f provides an estimate of the flow resistance reduction due to flow aeration. Chanson (1994) re-analyzed data from model studies and prototype tests to determine the apparent decrease in the Darcy-Weisbach friction factor for aerated flows:

$$\frac{f_a}{f} = 0.5\left(1 + \tanh\left(0.628\frac{0.514 - C_m}{C_m(1 - C_m)}\right)\right) \quad (8)$$

Figure 4b shows the present data of f_a/f as a function of C_m together with the experimental data of Straub and Anderson (1958) and prototype data compiled by Chanson (1994). The present data were in good agreement with these previous studies as well as with Eq. 8 for the range of the hydraulic roughness (0.5 mm $\lesssim k_s \lesssim 6$ mm) used in the calculation of the reference friction factor f. Note that empirical shape correction factors (e.g. after Schröder (1990)) to account for the unequal distribution of wall shear stress in partially filled pipe flow were not used as empirical corrections are only available for non-aerated, hydraulically smooth conditions. Applying the correction of (Schröder, 1990) would result in a $\approx 15\%$ reduction of
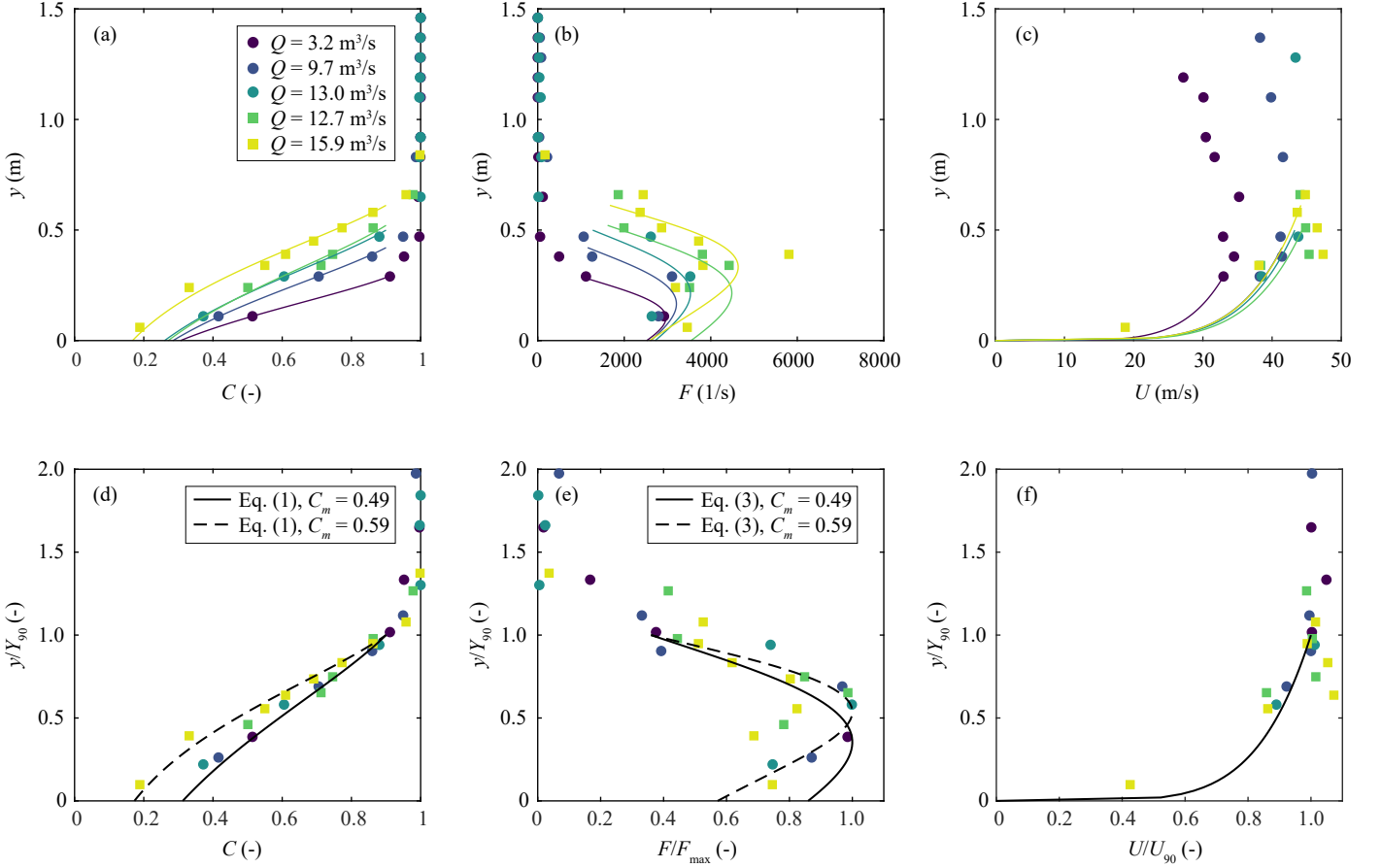
Figure 3: Basic air-water flow properties in dimensional ((a) to (c)) and non-dimensional form ((d) to (f)); (a) and (d) void fraction C compared to Eq. 1 (solid lines); (b) and (e) particle count rate F compared to Eq. 3 (solid lines); (c) and (f) interfacial velocity U compared to Eq. 4 with $n = 6$ (solid lines).

f_a/f indicating that effects of profile shape and unequal roughness distribution may contribute to the scatter in the prototype data in Fig. 4b. The good agreement of bulk air-water flow parameters with previous studies and empirical equations is an important finding since it suggests that laboratory scale studies may estimate important design parameters such as the flow aeration, side-wall height, residual energy at the downstream end and flow resistance accurately for $4.7 \cdot 10^5 \leq R \leq 2.4 \cdot 10^7$.

3.3. Particle size distribution

Particle size distributions are important to characterize air-water flows as mass, momentum and energy transfer processes are linked to the interfacial area (Chanson, 1997). Bubble and droplet sizes are governed by turbulent pressure forces at the scale of the particle and by surface tension (Deane and Stokes, 2002). Previous studies reported significant scale effects regarding bubble and droplet chord lengths (Felder and Chanson, 2009, 2017; Hohermuth, 2019). Therefore, the droplet size distributions of the present prototype measurements were analyzed in detail. The calculation of particle sizes in terms of a Sauter diameter $d_{32} = 1.5CU/F$ was not possible because for series T1 the measured F values were affected by the sampling frequency. Instead, the particle chord lengths (l_{ch}) were calculated as $l_{ch,i} = t_{ch,i}u_i$, where t_{ch} is the chord time, u_i is the interfacial velocity and subscript i denotes that $l_{ch,i}$ is calculated for

each ith correlation window separately (Kramer, 2019). The measured chord lengths were similar for the four plotted prototype flow conditions (Fig. 5a, data for $R = 2.2 \cdot 10^7$ from T2 is not shown as data for a comparable C are not available). Applying Froude scaling, exemplary chord lengths from a laboratory low-level outlet with similar local Froude numbers (F) and comparable C but smaller R (Hohermuth, 2019) are also included in Figure 5 for comparison. Note that these data were not collected in uniform flow conditions but in gradually varied decelerating flows (see Felder et al. (2019b) for information on the experimental setup). While the linear scale suggests a close agreement of all chord length distributions, the illustration in log-scale shows that a large portion of the distribution comprising the smaller l_{ch} was not detected for the prototype data for series T1 (Fig. 5d). As mentioned previously, this was linked with the sampling rate; the slightly larger minimum l_{ch} for series T2 are likely due to the larger probe size compared to the model tests. Illustrations in terms of dimensionless droplet chord lengths l_{ch}/d_c, show a clear tendency of the measured modes to shift towards smaller values for increasing R (Fig. 5b). This is even more apparent in log-scale, despite the truncation of the distributions from series T1 due to missing smallest chord lengths (Fig. 5e). A non-dimensional illustration with the median value ($l_{ch}/l_{ch,\text{median}}$), reveals a self-similar shape of

Table 2: Summary of results for all flow conditions.

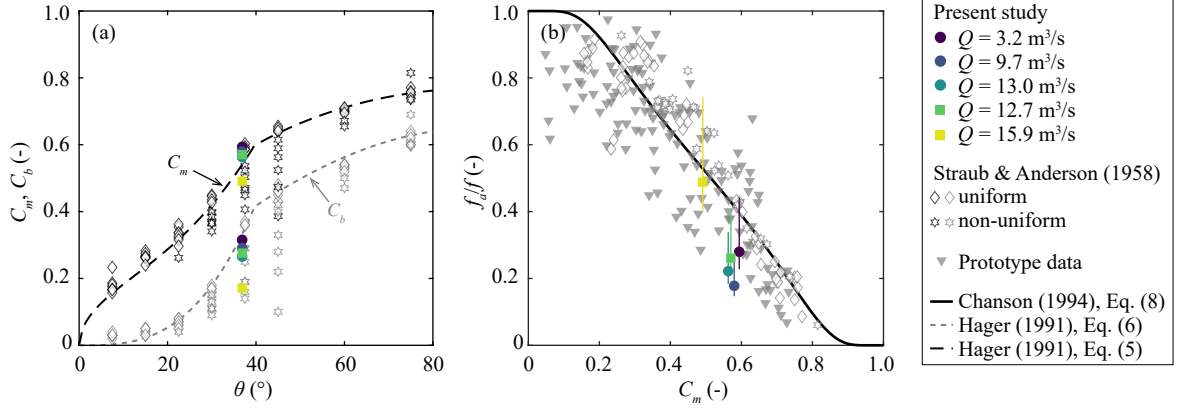| test series	Q_w	D' (Eq. 1)	C_m (Eq. 2)	Y_{90}	Y_w	R_h	$U_{m,w} = Q_w/A_w$	$\overline{U} = U_{90}\frac{n}{n+1}$	R
(-)	(m^3/s)	(-)	(-)	(m)	(m)	(m)	(m/s)	(m/s)	(-)
T1	3.2	0.57	0.59	0.28	0.15	0.10	23.3	28.2	$7.8 \cdot 10^6$
T1	9.7	0.55	0.58	0.42	0.23	0.15	38.4	35.5	$1.9 \cdot 10^7$
T1	13.0	0.52	0.56	0.50	0.28	0.18	38.5	37.1	$2.3 \cdot 10^7$
T2	12.7	0.53	0.57	0.52	0.29	0.19	35.9	38.3	$2.2 \cdot 10^7$
T2	15.9	0.41	0.49	0.61	0.38	0.24	30.3	37.9	$2.4 \cdot 10^7$

Figure 4: (a) Mean C_m and bottom C_b air concentration as a function of slope, comparison with Eqs. 5, 6 (Hager, 1991) and model data of Straub and Anderson (1958) ("uniform" and "non-uniform" after Wood (1991)); (b) f_a/f as a function of C_m, comparison with Eq. 8 (Chanson, 1994), model data of Straub and Anderson (1958) and prototype data re-analyzed by Chanson (1994). Markers denote k_s = 3 mm, error bars indicate the range of 0.5 mm $\lesssim k_s \lesssim$ 6 mm.

the right distribution tail across $1.8 \cdot 10^6 \leq R \leq 2.4 \cdot 10^7$ (Fig. 5c, f). As the distribution shape is indicative of the underlying fragmentation process (Villermaux, 2007), the observed agreement between laboratory and prototype scale may indicate that the droplet formation process is not fundamentally different at prototype conditions.

4. Discussion on scale effects

The present data of macroscopic and bulk air-water flow properties highlight the possibility to scale such laboratory data to prototype scale with $R \leq 2.4 \cdot 10^7$, expanding previous findings of laboratory scale studies of spillway flows (e.g. Boes and Hager (2003b); Felder and Chanson (2009, 2017); Hohermuth (2019)). Consequently, quantities of engineering interest such as bottom and depth-averaged air concentration, mixture flow depth, velocities and flow resistance can be estimated using existing empirical equations up to at least $R \leq 2.4 \cdot 10^7$.

Significant scale effects in terms of microscopic air-water flow properties such as droplet chord lengths were reported in previous studies (e.g. Felder and Chanson (2009, 2017); Hohermuth (2019)). The present observations, which showed a shift of the dimensionless droplet chord length distributions towards smaller values with increasing discharge and R respectively, extended these findings up to $R \leq 2.4 \cdot 10^7$. Effects of particle size may become important for mass transfer processes (e.g. oxygenation) and momentum transfer (e.g. air transport in the spray region $0.7 \lesssim C \leq 1$).

The Weber number (W) describes the ratio of differential pressure forces across the droplet and the restoring surface ten-

sion force (Hinze, 1955). W is typically used in the description of primary and secondary breakup of jets (Villermaux, 2007). Using theoretical analysis and experiments, Dai et al. (1998) found that the drop size in the turbulent primary breakup of liquid wall jets follows $d_{32}/L \propto W_L^{-3/5}$, where the streamwise integral length scale (L) approximated as $L = R_h/2$ is used in the formulation of $W_L = \rho_w U^2 L/\sigma$ with ρ_w water density and σ surface tension coefficient. To estimate the scaling of droplet chord lengths, the median relative droplet chord length is plotted as a function of Weber number in Fig 6. Due to the low sampling frequency in series T1 a significant portion of the smallest droplet chord lengths were not recorded and the measured median thus does not represent the true median. This affects the comparison to data collected with higher sampling frequency at laboratory scale. To overcome this, the full distributions were approximated with maximum likelihood estimates of a given truncated analytical distribution (Nadarajah and Kotz, 2006; Novomestky and Nadarajah, 2016). While drop size distributions are typically close to Gamma or log-normal distributions (Villermaux, 2007), the log-normal distribution was chosen herein as it was in better agreement with the measurements. The measured cumulative distribution function as well as the maximum likelihood estimate of the truncated distribution and the resulting reconstructed full distribution are shown in Fig. 6a. The resulting estimates of $l_{ch,\text{median}}$ calculated from the reconstructed full distribution were also plotted as solid symbols in Fig. 6 showing an improved agreement of the data with $l_{ch,\text{median}}/L \approx 55W_L^{-3/5}$. The data scatter may be partly attributed to the measurement uncertainty regarding
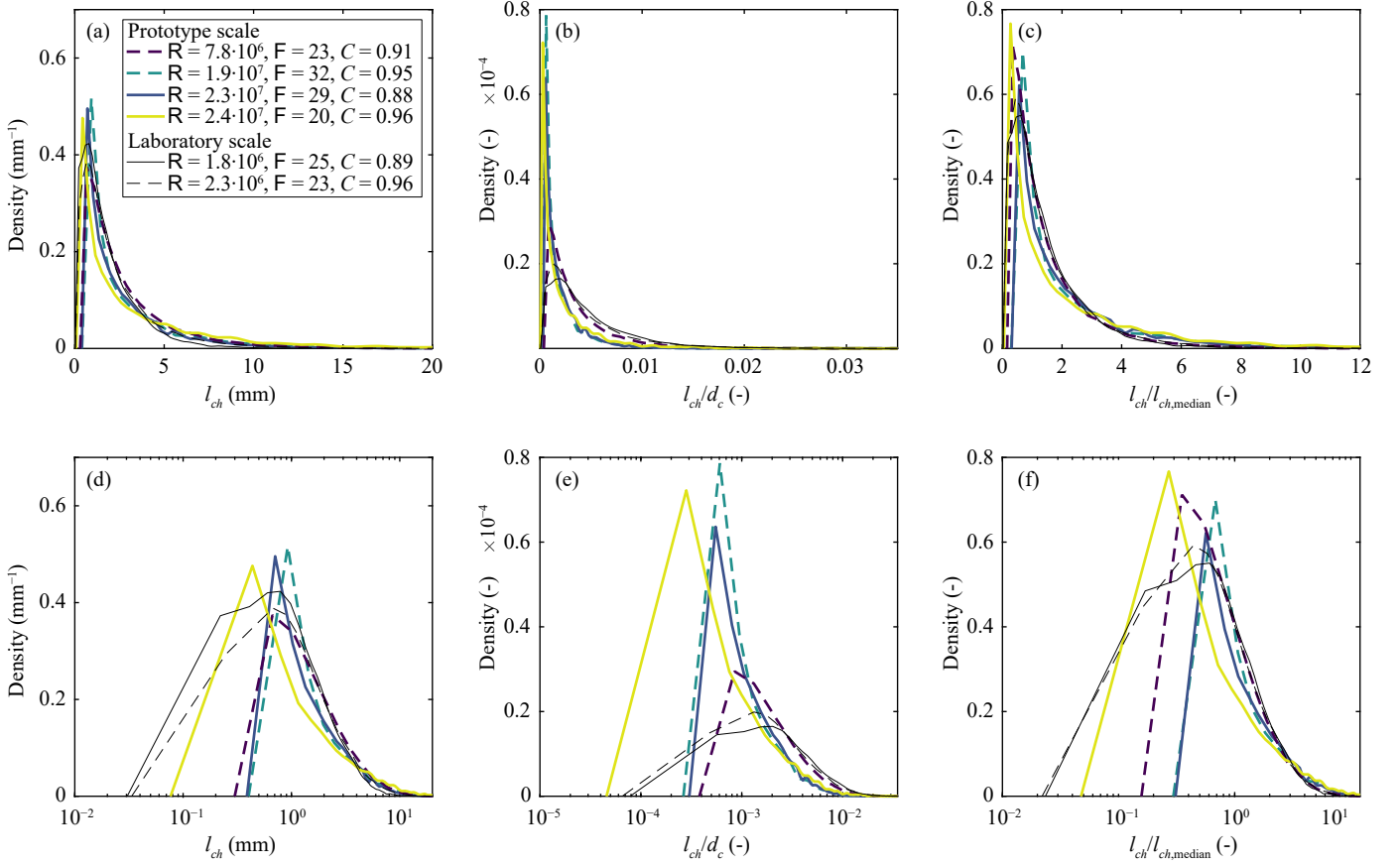
Figure 5: Kernel density estimates for measured droplet chord length distributions at different bulk Reynolds numbers. (a),(d) chord length; (b),(e) ratio of chord length to critical flow depth; (c),(f) ratio of chord length to median chord length. Laboratory scale measurements of Hohermuth (2019) at $R = 1.8 \cdot 10^6$, $R = 2.3 \cdot 10^6$ shown for comparison (thin black lines).

$l_{ch,\text{median}}$. More detailed and accurate measurements of droplet and bubble size distributions at prototype scale are necessary to corroborate the observed trend and draw quantitative conclusions. Nevertheless, the good agreement of the relative droplet chord length for the present prototype and laboratory data for $1.8 \cdot 10^6 \leq R \leq 2.4 \cdot 10^7$ with the trend $d_{32}/L \propto W_L^{-3/5}$ provide an explanation for the observed scale effects (Fig. 5). Applying Froude similitude leads to $W_M = W_P/\lambda^2$ where λ is the model scale and the subscripts $_{M,P}$ stand for model and prototype, respectively. Inserting the relation from Fig. 6b results in $l_{ch,\text{median},M}/L_M \approx l_{ch,\text{median},P}/L_P \, \lambda^{6/5}$, indicating that the relative droplet chord length in the model is overestimated with $\propto \lambda^{6/5}$. Further assuming that L is scaled correctly leads to $l_{ch,\text{median},M} \approx l_{ch,\text{median},P} \, \lambda^{1/5}$ which agrees with the overall trend in Fig. 5. However, more research, including model scale families, is needed to confirm this trend.

5. Conclusion

Two prototype tests were conducted in high-velocity air-water flows in the tunnel chute of Luzzone Dam. In each test series, an array of 16 double-tip conductivity probes recorded unique air-water flow data for four different discharges with Reynolds numbers of up to $2.4 \cdot 10^7$ and cross-sectional aver-

age flow velocities up to 38 m/s providing air-water flow data at the largest velocity yet. Distributions of void fraction, particle count rate and interfacial velocity followed existing semi-empirical distributions and several bulk parameters including the depth-average void fraction and flow resistance were consistent with previous smaller-scale studies and semi-empirical design equations. These finding highlighted the scalability of important engineering design parameters providing validation of previous laboratory scale testing. The mean void fraction was lower for higher discharges, identifying the effect of increasing flow depth (i.e. decreasing aspect ratio) on air-water flow properties as an area of future research. Regarding microscopic air-water flow properties, our results indicate that droplet sizes were not scaled correctly applying Froude scaling, which may affect predictions of air-water mass transfer processes within laboratory-scale air-water flows and momentum exchange processes of ejected droplets. However, more detailed particle size measurements at prototype scale are needed in order to quantify these effects. Due to violent impacts of the flow and debris, most conductivity probes were damaged during the measurement campaign and only limited data were recorded next to the chute invert. To limit the time the probes are exposed to the flow and to reduce the chance of debris impacts, future prototype measurements should consider the use of a robotic arm to
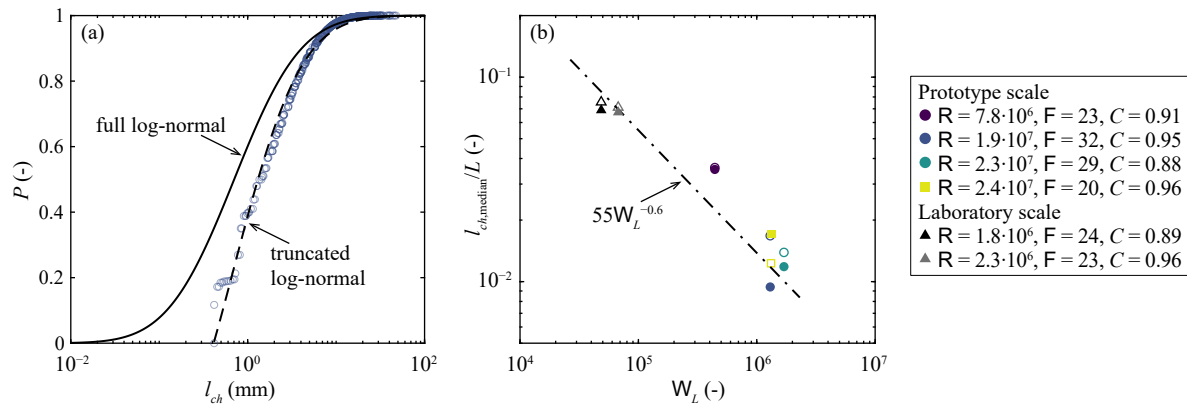
Figure 6: (a) Cumulative frequency distribution of measured chord lengths for $R = 1.8 \cdot 10^7$ compared to fitted truncated log-normal (dashed line) and reconstructed full distribution (solid line) (b) Scaling of median dimensionless chord length with Weber number. Hollow symbols = median from measured l_{ch} distribution, solid symbols = median from reconstructed full log-normal distribution.

move the probes in and out of the flow. Future prototype measurements should also focus on the near-invert region to provide missing data on the scalability of bubble sizes and to provide further validation for near-wall velocities and turbulence levels.

Data Availability Statement

Data generated or used during the study are available in a repository online in accordance with funder data retention policies (https://doi.org/10.3929/ethz-b-000482452).

References

Aivazyan, O.M., 1986. Stabilized aeration on chutes. Gidrotekhnicheskoe Stroitel'stvo, No. 12, 33-40. Translated in Hydrotechnical Construction, 1987, 713–722.

Auel, C., Albayrak, I., Boes, R.M., 2014. Turbulence characteristics in supercritical open channel flows: Effects of froude number and aspect ratio. Journal of Hydraulic Engineering 140, 04014004. doi:10.1061/(ASCE)HY.1943-7900.0000841.

Boes, R., 2000. Zweiphasenströmung und Energieumsetzung an Grosskaskaden (two-phase flow and energy dissipation on stepped spillways, in German). Ph.D. thesis. Labortatory of Hydraulics, Hydrology and Glaciology (VAW), ETH Zurich. Zurich, Switzerland.

Boes, R.M., Hager, W.H., 2003a. Hydraulic design of stepped spillways. Journal of Hydraulic Engineering 129, 671–679. doi:10.1061/(ASCE)0733-9429(2003)129:9(671).

Boes, R.M., Hager, W.H., 2003b. Two-phase flow characteristics of stepped spillways. Journal of Hydraulic Engineering 129, 661–670. doi:10.1061/(ASCE)0733-9429(2003)129:9(661).

Brocchini, M., Peregrine, D.H., 2001. The dynamics of strong turbulence at free surfaces. part 1. description. Journal of Fluid Mechanics 449, 225–254.

Cain, P., 1978. Measurements within self-aerated flow on a large spillway. Ph.D. thesis. University of Canterbury. Christchurch, New Zealand.

Cain, P., Wood, I.R., 1981. Measurements of self-aerated flow on a spillway. Journal of the Hydraulics Division 107, 1425–1444.

Chanson, H., 1994. Drag reduction in open channel flow by aeration and suspended load. Journal of Hydraulic Research 32, 87–101. doi:10.1080/00221689409498791.

Chanson, H., 1997. Air Bubble Entrainment in Free-surface Turbulent Shear Flows. Academic Press.

Chanson, H., 2015. Energy dissipation in hydraulic structures, in: Chanson, H. (Ed.), IAHR Monograph, CRC Press, Taylor & Francis Group, Leiden, The Netherlands.

Chanson, H., Brattberg, T., 2000. Experimental study of the air-water shear flow in a hydraulic jump. International Journal of Multiphase Flow 26, 583–607.

Chanson, H., Chachereau, Y., 2013. Scale effects affecting two-phase flow properties in hydraulic jump with small inflow froude number. Experimental Thermal and Fluid Science 45, 234–242. doi:https://doi.org/10.1016/j.expthermflusci.2012.11.014.

Chanson, H., Gualtieri, C., 2008. Similitude and scale effects of air entrainment in hydraulic jumps. Journal of Hydraulic Research 46, 35–44. doi:10.1080/00221686.2008.9521841.

Chanson, H., Toombes, L., 2002. Air–water flows down stepped chutes: turbulence and flow structure observations. International Journal of Multiphase Flow 28, 1737–1761.

Dai, Z., Chou, W.H., Faeth, G.M., 1998. Drop formation due to turbulent primary breakup at the free surface of plane liquid wall jets. Physics of Fluids 10, 1147–1157. doi:10.1063/1.869639.

Deane, G.B., Stokes, M.D., 2002. Scale dependence of bubble creation mechanisms in breaking waves. Nature 418, 839–844.

Felder, S., Chanson, H., 2009. Turbulence, dynamic similarity and scale effects in high-velocity free-surface flows above a stepped chute. Experiments in Fluids 47, 1 – 18. doi:https://doi.org/10.1007/s00348-009-0628-3.

Felder, S., Chanson, H., 2015a. Aeration and air–water mass transfer on stepped chutes with embankment dam slopes. Environmental Fluid Mechanics 15, 695–710.

Felder, S., Chanson, H., 2015b. Phase-detection probe measurements in high-velocity free-surface flows including a discussion of key sampling parameters. Experimental and Thermal Fluid Science 61, 66–79.

Felder, S., Chanson, H., 2016a. Air–water flow characteristics in high-

velocity free-surface flows with 50% void fraction. International Journal of Multiphase Flow 85, 186 – 195. doi:https://doi.org/10.1016/j.ijmultiphaseflow.2016.06.004.

Felder, S., Chanson, H., 2016b. Simple design criterion for residual energy on embankment dam stepped spillways. Journal of Hydraulic Engineering 142, 04015062. doi:10.1061/(ASCE)HY.1943-7900.0001107.

Felder, S., Chanson, H., 2017. Scale effects in microscopic air-water flow properties in high-velocity free-surface flows. Experimental Thermal and Fluid Science 83, 19 – 36. doi:https://doi.org/10.1016/j.expthermflusci.2016.12.009.

Felder, S., Geuzaine, M., Dewals, B., Erpicum, S., 2019a. Nappe flows on a stepped chute with prototype-scale steps height: Observations of flow patterns, air-water flow properties, energy dissipation and dissolved oxygen. Journal of Hydro-environment Research 27, 1 – 19. doi:https://doi.org/10.1016/j.jher.2019.07.004.

Felder, S., Hohermuth, B., Boes, R.M., 2019b. High-velocity air-water flows downstream of sluice gates including selection of optimum phase-detection probe. International Journal of Multiphase Flow 116, 203–220.

Hager, W.H., 1991. Uniform aerated chute flow. Journal of Hydraulic Engineering 117, 528–533. doi:10.1061/(ASCE)0733-9429(1991)117:4(528).

Hall, L.S., 1943. Open channel flow at high velocities. Transactions ASCE 108, 1394–1434.

Hartung, F., Scheuerlein, H., 1970. Design of overflow rockfill dams, in: Proceedings, 10th ICOLD Congress, Montreal, Q36, R35, 587–596.

Heller, V., 2011. Scale effects in physical hydraulic engineering models. Journal of Hydraulic Research 49, 293–306. doi:10.1080/00221686.2011.578914.

Hinze, J.O., 1955. Fundamentals of the hydrodynamic mechanism of splitting in dispersion processes. AIChE Journal 1, 289–295. doi:https://doi.org/10.1002/aic.690010303.

Hohermuth, B., 2019. Aeration and two-phase flow characteristics of low-level outlets. Ph.D. thesis. Laboratory of Hydraulics, Hydrology and Glaciology, ETH Zurich, Switzerland. Zurich, Switzerland. doi:https://doi.org/10.3929/ethz-b-000351715.

Hunt, S.L., Kadavy, K.C., Hanson, G.J., 2014. Simplistic design methods for moderate-sloped stepped chutes. Journal of Hydraulic Engineering 140, 04014062. doi:10.1061/(ASCE)HY.1943-7900.0000938.

Keller, R.J., 1972. Field Measurement of Self-Aerated High Speed Open Channel Flow. Ph.D. thesis. University of Canterbury. Christchurch, New Zealand.

Keller, R.J., Lai, K.K., Wood, I.R., 1974. Developing region in self-aerated flows. ASCE Journal of the Hydraulics Division 100.

Kobus, H., 1984. Scale effects in modelling hydraulic structures, in: Kobus, H. (Ed.), Proceedings of the International Symposium Scale Effects in Modelling Hydraulic Structures, Esslingen, Germany.

Kramer, K., Hager, W.H., Minor, H.E., 2006. Development of air concentration on chute spillways. Journal of Hydraulic Engineering 132, 908–915. doi:10.1061/(ASCE)0733-9429(2006)132:9(908).

Kramer, M., 2019. Particle size distributions in turbulent air-water flows, in: Proc. 38th IAHR World Congress, Panama City, IAHR. pp. 5722–5731. doi:doi:10.3850/38WC092019-0680.

Kramer, M., Hohermuth, B., Valero, D., Felder, S., 2020. Best practices for velocity estimations in highly aerated flows with dual-tip phase-detection probes. International Journal of Multiphase Flow 126, 103228. doi:https://doi.org/10.1016/j.ijmultiphaseflow.2020.103228.

Kramer, M., Hohermuth, B., Valero, D., Felder, S., 2021. On velocity estimations in highly aerated flows with dual-tip phase-detection probes - closure. International Journal of Multiphase Flow 134, 103475. doi:https://doi.org/10.1016/j.ijmultiphaseflow.2020.103475.

Kramer, M., Valero, D., Chanson, H., Bung, D.B., 2019. Towards reliable turbulence estimations with phase-detection probes: an adaptive window cross-correlation technique. Experiments in Fluids 60:2, 6 pages.

Matos, J., 2000. Hydraulic design of stepped spillways over rcc dams, in: H.E., M., W.H., H. (Eds.), International Workshop on Hydraulics of Stepped Spillways, Zürich, Switzerland, Balkema. pp. 187–194.

Nadarajah, S., Kotz, S., 2006. R programs for truncated distributions. Journal of Statistical Software, Code Snippets 16, 1–8. URL: https://www.jstatsoft.org/v016/c02, doi:10.18637/jss.v016.c02.

Novomestky, F., Nadarajah, S., 2016. truncdist: Truncated Random Variables. URL: https://CRAN.R-project.org/package=truncdist. r package version 1.0-2.

Pagliara, S., Carnacina, I., Roshni, T., 2010. Air-water flows in the presence of staggered and row boulders under macroroughness conditions. Water Resources Research 46. doi:10.1029/2009WR008834.

Pfister, M., Chanson, H., 2012. Discussion to scale effects in physical hydraulic engineering models by valentin heller, journal of hydraulic research, vol. 49, no. 3 (2011), pp. 293–306. Journal of Hydraulic Research 50, 244–246. doi:10.1080/00221686.2012.654671.

Pfister, M., Chanson, H., 2014. Two-phase air-water flows: Scale effects in physical modeling. Journal of Hydrodynamics, Ser. B 26, 291–298. doi:https://doi.org/10.1016/S1001-6058(14)60032-9.

Pujol, A., Lopardo, R., Vernet, G.F., Tatone, G., Chividini, M.F., Larrea, J.C., Henning, R.E., 1985. Incorporacion de aire y presiones fluctuantes en el aliviadero de la presa alicura. Secretary of Hydraulic Resources, National Institute of Science and Hydraulic Engineering, Applied Hydraulic Laboratory, Argentina.

Schröder, R., 1990. Hydraulische Methoden zur Erfassung von Rauheiten (Hydraulic methods to determine roughnesses). Technical Report Schrift 92. DVWK. Hamburg and Berlin.

Speerli, J., 1999. Strömungsprozesse in Grundablassstollen (Hydraulics of low-level outlets, in German). Ph.D. thesis. VAW-Report 163, Laboratory of Hydraulics, Hydrology and Glaciology (VAW), ETH Zurich. Zurich, Switzerland.

Speerli, J., Hager, W.H., 2000. Air-water flow in bottom outlets. Canadian Journal of Civil Engineering 27, 454–462. doi:10.1139/l99-087.

Straub, L.G., Anderson, A.G., 1958. Experiments on self-aerated flow in open channels. Journal of the Hydraulics Division 84, 1–35.

Toro, J.P., Bombardelli, F.A., Paik, J., 2017. Detached eddy simulation of the nonaerated skimming flow over a stepped spillway. Journal of Hydraulic Engineering 143, 04017032. doi:10.1061/(ASCE)HY.1943-7900.0001322.

Valero, D., Bung, D.B., 2018. Reformulating self-aeration in hydraulic structures: Turbulent growth of free surface perturbations leading to air entrainment. International Journal of Multiphase Flow 100, 127–142.

Vernet, G., Angelaccio, C., Chividini, M., 1988. Model-prototype comparison in the alicura chute spillway air system, in: Burgi, P.H. (Ed.), Model-prototype correlation of hydraulic structures: proceedings of the International Symposium sponsored by the Hydraulics Division of the American Society of Civil Engineers, Colorado Springs, Colorado, August 9-11, American Society of Civil Engineers, New York, USA.

Villermaux, E., 2007. Fragmentation. Annual Review of Fluid Mechanics 39, 419–446. URL: https://doi.org/10.1146/annurev.fluid.39.050905.110214, doi:10.1146/annurev.fluid.39.050905.110214.

Volkart, P., Rutschmann, P., 1984. Rapid flow in spillway chutes with and without deflectors - a model-prototype comparison, in: Kobus, H. (Ed.), Symposium on Scale Effects in Modelling Hydraulic Structures, Esslingen am Neckar, Germany, Technische Akademie Esslingen. pp. 4.5–1 to 4.5–7.

Wang, H., Chanson, H., 2016. Self-similarity and scale effects in physical modelling of hydraulic jump roller dynamics, air entrainment and turbulent scales. Environmental Fluid Mechanics 16, 1087–1110. doi:10.1061/10.1007/s10652-016-9466-z.

Wood, I.R., 1991. Air entrainment in free-surface flows. IAHR Hydraulic Structures Design Manual 4, Taylor & Francis.

Zünd, B., 2008. Fliesswiderstand eines belüfteten Freispiegelabflusses im Gleichgewichtszustand (Flow resistance of uniform aerated free-surface flow, in German). Ph.D. thesis. Labortatory of Hydraulics, Hydrology and Glaciology (VAW), ETH Zurich. Zurich, Switzerland.